Hyperboloidal slices for the wave equation of Kerr–Schild metrics and numerical applications

2012 Class. Quantum Grav. 29 015008

(http://iopscience.iop.org/0264-9381/29/1/015008)

IOP Publishing Classical and Quantum Gravity

Class. Quantum Grav. **29** (2012) 015008 (15pp) doi:10.1088/0264-9381/29/1/015008

Hyperboloidal slices for the wave equation of Kerr–Schild metrics and numerical applications

Michael Jasiulek

Max-Planck-Institut für Gravitationsphysik, Albert-Einstein-Institut, Am Mühlenberg∼1, D-14476 Golm, Germany

E-mail: michaelj@aei.mpg.de

Received 13 September 2011, in final form 27 October 2011
Published 13 December 2011
Online at stacks.iop.org/CQG/29/015008

Abstract

We present new results from two codes, using finite differencing and pseudo-spectral methods for the wave equations in (3+1) dimensions. We use a hyperboloidal transformation, which allows direct access to null infinity and simplifies the control over characteristic speeds on Kerr–Schild backgrounds. We show that this method is ideal for attaching hyperboloidal slices or for adapting the numerical resolution in certain spacetime regions. As an example application, we study late-time Kerr tails of sub-dominant modes and obtain new insight into the splitting of decay rates. The involved conformal wave equation is freed of formally singular terms whose numerical evaluation might be problematically close to future null infinity.

PACS numbers: 04.25.D−, 03.65.Pm, 04.20.Ex, 04.30.−w

1. Introduction

In the recent past, since the work of [1–3], hyperboloidal slicings have been used frequently for numerical computations in general relativity as an elegant solution to the outer boundary and the radiation extraction problem by including null infinity in the slicing [4]. The applications range from time-domain simulations of the scalar wave equation on Minkowski, Schwarzschild [3, 5] and Kerr backgrounds [6, 7] to compute quasi-normal-mode oscillations, to study the late-time behaviour of the solution, to study the influence of nonlinear source terms, to compute the scalar self-force of point particles orbiting a Schwarzschild black hole [8] and to compute gravitational waveforms from extreme-mass-ratio inspirals [9, 10]. A new and interesting idea is to apply the framework to perturbation equations in the frequency domain [11]. Recently, the use of hyperboloidal slices even allowed the Einstein equations to evolve in axisymmetry including null infinity; see [12] and references therein.

The spatial domain in the numerical solution of hyperbolic PDEs is typically truncated at a finite coordinate distance, where artificial outer-boundary conditions are imposed and the outgoing radiation of the test field is extracted. This practice causes certain well-known conceptual and practical difficulties, such as artificial reflections on the outer boundary, which

can destroy relevant features of the solution. In this context, the use of hyperboloidal slicings offers an alternative by including the physical boundary $\mathscr{I}^+$ on the numerical grid.

Many numerical applications require a specific coordinate system in a compact domain and it is necessary to attach hyperboloidal coordinates at some transition point. In the original work [1], this was accomplished by introducing a transition zone, which required the fine tuning of many parameters for the chosen transition function and a disadvantageous hyperboloidal transformation, which had a suitable asymptotic behaviour but caused the outgoing characteristic speed to drop in the transition region. This led to numerical problems in subsequent works [5, 6, 8]. In the recent work [10], appearing during the completion of this paper, the authors present a solution to the problem.

For this paper, we developed a finite differencing (FD) and a pseudo-spectral (PS) code in (3+1) dimensions to test a new hyperboloidal transformation that simplifies the control over characteristic speeds for the first-order reduced wave equation on Kerr–Schild backgrounds. Thereby, we can avoid the above-mentioned problem by requiring the outgoing characteristic speed to be invariant under the compactifying hyperboloidal transformation. We demonstrate this by performing a numerical comparison with the attached hyperboloidal slices as originally used in [1]. As an example application, we investigate the late-time decay rates in Kerr at the horizon, finite radii and null infinity and study the m-dependence of the splitting of certain sub-dominant modes, which was found in the numerical studies of [6, 7]. More technically, we remove formally singular terms that appear in the conformal wave equation that might numerically be problematic to evaluate at the outer boundary $\mathscr{I}^+$, where the conformal factor vanishes. Our framework is general enough to cover metrics of the Kerr–Schild form. Thus, our approach could be applied in the numerical analysis of quasi-normal modes in Vaidya [13], and more generally, in time-dependent non-axisymmetric Kerr–Schild spacetimes.

The infrastructure and implementations we present here are comprehensive, allowing standard coordinates in the spacetime interior in (3+1), smooth matching of hyperboloidal slices and covering the large class of Kerr–Schild metrics with FD and PS techniques. A comparable work is [5] in which Minkowski and Schwarzschild backgrounds are treated on hyperboloidal slices in (3+1) with PS techniques using the aforementioned non-optimal transition zone.

The paper is organized in the following way. In section 2, we introduce our notation and convention of Kerr–Schild metrics and the scalar wave equation. In section 3, we briefly explain the hyperboloidal method as well as the particular hyperboloidal transformation we employed. Then, we compare the resulting characteristic coordinate speeds and the scalar curvature for matched hyperboloidal slices with other methods. In section 4, we apply our method to solve the scalar wave equation with FD. In section 5, we explain implementational details and compare different matching methods numerically. We then proceed to explain the PS code and use this on a single hyperboloidal domain (no matching) to study polynomial decay rates of sub-dominant modes on Kerr.

Note that we use a tilde as in $\tilde{r}$ or $\tilde{g}^{\mu\nu}$ to denote compactified hyperboloidal coordinates and components of tensors. Conformally rescaled tensors are denoted by the superscript Ω as in ${}^{\Omega}l^{\mu} = l^{\mu}/\Omega$ or ${}^{\Omega}g^{\mu\nu} = g^{\mu\nu}/\Omega^2$. Derivatives w.r..t the Kerr–Schild radius r are denoted by a prime like $\mathrm{d}h/\mathrm{d}r = h'$ and w.r.t. the rescaled radius $\tilde{r}$ by a dot like $\mathrm{d}h/\mathrm{d}\tilde{r} = \dot{h}$.

2. Wave equation in Kerr–Schild coordinates

2.1. Kerr–Schild metrics and Kerr metric

Kerr–Schild metrics are of the general form

$$g^{\mu\nu} = \eta^{\mu\nu} - 2V(t, x^i)\, l^{\mu} l^{\nu}, \tag{1}$$

where $\eta^{\mu\nu} = \mathrm{diag}(-1, 1, 1, 1)$ is the flat metric, (t, x^i) are the Kerr–Schild coordinates and l^μ is a null vector w.r.t. $\eta^{\mu\nu}$ ($\Rightarrow g^{\mu\nu} l_\mu l_\nu = 0$) of the form

$$l^\mu = (-1,\ l^i), \quad k^\mu = (1, l^i) - 2V\, l^\mu \tag{2}$$

and k^μ is the second null vector normalized to $k^\mu l_\mu = 2$ ($\Leftrightarrow l^i l^j \delta_{ij} = 1$). l^i and V[1] are free functions that characterize the Kerr–Schild metric in question.

In Kerr with mass M and angular momentum $a\,M$, we have

$$V(x^i) = M\frac{r_{\mathrm{BL}}}{s} \quad \left(= \frac{M}{2}\nabla_\mu l^\mu\right), \tag{3}$$

where $s := \sqrt{(r^2 - a^2)^2 + (2az)^2}$, $r_{\mathrm{BL}} = \frac{1}{\sqrt{2}}\sqrt{r^2 - a^2 + s}$ is the Boyer–Lindquist radius and $r = \sqrt{x^2 + y^2 + z^2}$ the Kerr–Schild radius, and

$$l^i = \left(\frac{r_{\mathrm{BL}} x + a\, y}{{r_{\mathrm{BL}}}^2 + a^2}, \frac{r_{\mathrm{BL}} y - a\, x}{{r_{\mathrm{BL}}}^2 + a^2}, \frac{z}{r_{\mathrm{BL}}}\right). \tag{4}$$

Then, $(-l^\mu)$ is the future-directed ingoing principal null vector and k^μ is the outgoing one. With our sign convention

$$n \cdot l = +\frac{r_{\mathrm{BL}}}{r}, \tag{5}$$

where $n \cdot l := n_\mu l^\mu$ and $n_i = n^i = x^i/r$ is the radial unit normal. Note that l^μ is affinely parametrized, i.e. $l^\mu \nabla_\mu l^\nu = 0$. Sometimes it can be useful to work with $\hat{l}^\mu := \sqrt{2V} l^\mu$. Then, $\hat{l}^\mu\, \nabla_\mu \hat{l}^\nu = \phi\, \hat{l}^\nu = \partial_l V\, l^\nu = M\frac{a^2 - r^2}{s^2}\sqrt{\frac{1}{2V}}\, \hat{l}^\nu$.

2.2. *Wave equation in the first-order form*

The hyperboloidal method, explained in the next section, includes a conformal rescaling of the metric. Therefore, we consider the conformal wave equation instead of $\Box\, \Psi = 0$.[2]

We reduce the conformal wave equation

$$\left(\Box - \tfrac{1}{6}\mathcal{R}\right)\psi = g^{\mu\nu}\partial_\mu \psi_\nu - \Gamma^\mu(g)\psi_\mu - \tfrac{1}{6}\mathcal{R}\psi = 0 \tag{6}$$

to the first-order form by introducing the new variables $\psi_\nu := \partial_\nu \psi$, where $\Gamma^\lambda(g) := g^{\mu\nu}\Gamma^\lambda_{\mu\nu}$ are the contracted Christoffel symbols and $\mathcal{R}$ is the scalar curvature of $g^{\mu\nu}$. In general, $\Gamma^\mu = (\nabla_\mu \hat{l}^\mu + \phi)\, \hat{l}^\mu$ holds for metrics of the form (1). In Kerr, it can be shown that

$$\Gamma^\mu(g) = \frac{2M}{s} l^\mu. \tag{7}$$

This leads to the following system of evolution equations for the variables $\{\psi_{\nu=0,1,2,3}, \psi\}$: $\partial_0 \psi = \psi_0$, $\partial_0 \psi_j = \partial_j \psi_0$ and

$$-g^{00}\partial_0 \psi_0 = 2g^{0i}\partial_i \psi_0 + g^{ij}\partial_i \psi_j - \Gamma^\mu(g)\psi_\mu - \tfrac{1}{6}\mathcal{R}\psi \tag{8}$$

which is symmetric hyperbolic. For FD implementations of (8), the following flux-conservative form is more convenient for the long-term stability of the numerical evolution

$$-g^{00}\partial_0 \psi_0 = g^{0i}\partial_i \psi_0 + \frac{1}{\sqrt{g}}\partial_i F^i - \frac{1}{6}\mathcal{R}\psi, \quad \text{where} \tag{9}$$

$$F^i := \sqrt{g}\left(g^{0i}\psi_0 + g^{ij}\psi_j\right). \tag{10}$$

Here, finite differences are taken of ψ_0 and F^i instead of differentiating the evolution variables ψ_0 and ψ_i directly. This, in turn, is more efficient if spectral methods are used to compute spatial derivatives and equation (8) is preferred in that case.

[1] We assume asymptotic flatness, such that $V = M/r(1 + V_1/r + \mathcal{O}(1/r^2))$ and $l^i n_i = 1 + n \cdot l_1/r + \mathcal{O}(1/r^2)$, $n^i = x^i/r$. In Kerr, e.g., $V = M/r(1 + \mathcal{O}(1/r^2))$ and $n \cdot l = 1 - a^2/2(1 - (n_z)^2)/r^2 - \mathcal{O}(1/r^4)$.

[2] The scalar wave equation $\Box\, \psi = 0$ is per se not conformally invariant, i.e. a rescaled solution ${}^\Omega\psi := \psi/\Omega$ is in general not a solution of the wave equation of the rescaled metric ${}^\Omega g^{\mu\nu} := g^{\mu\nu}/\Omega^2$; see, e.g., appendix D of [14]. Note that $\mathcal{R} = 0$ holds for Kerr–Schild metrics, where l^μ is geodesic like in Kerr or Vaidya spacetimes.

3. Hyperboloidal method

Having explained the wave equation on Kerr–Schild backgrounds, we are now ready to describe the hyperboloidal method in the following section based on [1]. We explain the steps necessary to transform a given spacetime metric $g^{\mu\nu}$ in coordinates (t, x^i) and its t-slicing ($t =$ constant hypersurfaces) to a conformal metric ${}^{\Omega}\tilde{g}^{\mu\nu}$ in radially compactified hyperboloidal coordinates $(\tilde{t}, \tilde{x}^i)$ and its hyperboloidal $\tilde{t}$-slicing. It is often desirable to leave the coordinates (t, x^i) untouched in the spacetime interior, *inner domain*, and attach the *hyperboloidal domain* smoothly at some transition point r_{TR}. The hyperboloidal method we employ consist of three transformations, a radial compactification and a conformal rescaling of the metric

$$\tilde{x}^j = \Omega(r)\, x^j \quad \text{with} \quad \Omega = 0, \qquad \dot{\Omega} \neq 0 \text{ at } \mathscr{I}^+ \tag{11}$$

$${}^{\Phi}g_{\mu\nu} = \Phi^2 g_{\mu\nu} \quad \text{with} \quad \Phi \sim \Omega \text{ at } \mathscr{I}^+ \tag{12}$$

where $\dot{\Omega} := \mathrm{d}\Omega/\mathrm{d}\tilde{r}$ and we assume Ω and Φ to be non-negative. For simplicity, we set $\Omega \equiv \Phi$ in the following; see appendix B for $\Omega \neq \Phi$. The conformal transformation extends the spacetime to include $\mathscr{I}^+$ as its boundary [4] such that the conformal metric is regular there. For constant time slices to intersect $\mathscr{I}^+$, we require the additional transformation

$$\tilde{t} = t - h(r) \quad \text{with} \quad -\frac{I - 2n\cdot lV}{1 - 2n\cdot l^2 V} < h' < \frac{I + 2n\cdot lV}{1 - 2n\cdot l^2 V} \tag{13}$$

where the height function $h(r)$ possesses a carefully chosen asymptotic singular behaviour to allow $\tilde{t}$-slices to penetrate $\mathscr{I}^+$, similar to time transformations from Schwarzschild slicing to horizon penetrating slicings; see, e.g., figure 2 in [15] for illustration purposes. The restrictions on $h(r)$ in (13) are necessary for the hyperboloidal slices to be spacelike, where $h' := \mathrm{d}h/\mathrm{d}r$ and $I := \sqrt{1 + 2V(1 - n\cdot l^2)}$.

3.1. Controlling the coordinate speed of in/outgoing characteristics

In numerical applications of the hyperboloidal method, like for the hyperbolic system (8), it is often necessary to limit the ratio $\frac{\Delta t}{\Delta r}$ to obtain a stable numerical evolution, where Δr is the spatial grid spacing and Δt is the time step. This is the case, if the method of lines (MoL) and explicit time integration is used. Then, the CFL-condition must hold $c(r)\,\frac{\Delta t}{\Delta r} \leqslant \nu_{\mathrm{CFL}}$, where $c(r)$ is the coordinate speed of characteristics of the solution, explained in the following, and ν_{CFL} is the so-called Courant number that is independent of the solution. Therefore, an efficient numerical computation is limited by $\max\, c(r)$ and computing time may be wasted in regions, where $c(r) < \max\, c(r)$. On the other hand, it may be useful to obtain more temporal resolution in certain regions, e.g., to resolve a particular feature of the solution or to increase the accuracy there. In the following, we bring the height-function derivative $h'(r)$ in a particular form, which allows to directly specify the outgoing characteristic speed $c(r)$ as a function of radius in the hyperboloidal transformation, i.e. $h'(r) \to h'(r, c(r))$ independent of Ω. We also show how to use this feature for attaching hyperboloidal slices to an inner domain[3].

The in/outgoing characteristic speeds in the direction n_i of a hyperbolic system of the form $\partial_t U = A^i \partial_i U + BU$, where we assume that U is vector valued and A^i, B are matrices, are given by two eigenvalues of $A^i n_i$. For the systems (8) and (9), they are

$$\begin{aligned} c^{\pm}(g) :&= (-g^{0n} \pm \sqrt{(g^{0n})^2 - g^{00}\, g^{nn}})/(-g^{00}), \\ &= \frac{\pm I - 2Vn\cdot l}{1 + 2V} \quad \overset{n\cdot l \to 1}{\longrightarrow} \quad \frac{+1 - 2V}{1 + 2V}; -1 \end{aligned} \tag{14}$$

[3] As mentioned in the introduction in the recent work [10], this problem is solved in a slightly different way. The authors do not explicitly consider the characteristic speeds but guarantee a smooth transition of inner and hyperboloidal coordinates through $t_{\mathrm{BL}} - r^*_{\mathrm{BL}} = \tilde{t} - \tilde{r}$; see equation (7) of [10], where t_{BL} and r^*_{BL} are the Boyer–Lindquist time and tortoise radius, respectively.

where $g^{0n} = g^{0i}n_i$. We considered the limit $n \cdot l \to 1$ because in most parts of asymptotically flat spacetimes, see footnote 1, the two unit normals are almost aligned $n \cdot l \approx 1$, e.g., in extremal Kerr for $r > 1.2$. Instead of proceeding with the straightforward but long algebraic operations to simplify $c^{\pm}({}^{\Omega}\tilde{g})$, we proceed in a more intuitive way by considering the characteristic speeds of the first-order equation

$$l^{\mu}\partial_{\mu}\psi = 0 \tag{15}$$

which applies to the characteristics of the PDEs (8) and (9). Characteristics propagate on null rays of the background along which the solution is constant. The radial characteristic speeds of equation (15) along the null vectors $(-l^{\mu})$and k^{μ}, see equation (2), are

$$c^{(k)} = k^i n_i/k^0 = n \cdot l\frac{1-2V}{1+2V} \quad \overset{n\cdot l\to 1}{\longrightarrow} \quad c^{(k)} \equiv c^{+}(g), \tag{16}$$

$$c^{(l)} = l^i n_i/l^0 = -n \cdot l \quad \overset{n\cdot l\to 1}{\longrightarrow} \quad c^{(l)} \equiv c^{-}(g). \tag{17}$$

Under the compactifying hyperboloidal transformations (11) and (13), $c^{(k)}$ and $c^{(l)}$ change as

$$c^{(\tilde{k})} = n \cdot l\frac{1-2V}{1+2V}\frac{\Omega^2 L}{1-h'\frac{1-2V}{1+2V}n \cdot l} \quad \overset{n\cdot l\to 1}{\longrightarrow} \quad c^{(\tilde{k})} \equiv c^{+}(\tilde{g}), \tag{18}$$

$$c^{(\tilde{l})} = -n \cdot l\frac{\Omega^2 L}{1+h'n \cdot l} \quad \overset{n\cdot l\to 1}{\longrightarrow} \quad c^{(\tilde{l})} \equiv c^{-}(\tilde{g}), \tag{19}$$

where $L := \frac{\tilde{r}'}{\Omega^2} = \frac{1}{\Omega - \Omega\tilde{r}}$. From equation (19), we can see that conditions (11) on Ω and $\dot{\Omega}$ make $c^{(\tilde{l})}$ vanish at $\mathscr{I}^+$ (no ingoing characteristics). Equation (18) shows that to make $c^{(\tilde{k})}$ non-vanishing at $\mathscr{I}^+$, h' has to be of the form

$$h' = \frac{1+2V}{1-2V}(1-\Omega^2 LH) \quad \overset{h'=h'(r)}{\longrightarrow} \quad \frac{1+2\hat{V}(r)}{1-2\hat{V}(r)}(1-\Omega^2 LH(r)), \tag{20}$$

where $\hat{V}(r)$ is $V(x^i)$ along some arbitrary direction or some approximation. For practical purposes, it is enough to consider the leading order term of $V(x^i)$, i.e. $\hat{V}(r) = 2M/r$, as we do in the following. H is a free function in the range from zero to one to modify the coordinate speeds in the hyperboloidal domain. The spacelike condition (13) is guaranteed by h' of the above form, since $LH > 0$ by definition[4]. A simple choice might be $H = 1$. However, H allows direct access to the characteristic speed $c^{(\tilde{k})} = (1-2V)/(1+2V)\,1/H$ equation (18) and it is more convenient to require

$$c^{(\tilde{k})} = c^{(k)} \quad \overset{n\cdot l\to 1}{\Longrightarrow} \quad H(\tilde{r}) = \frac{1-2\hat{V}(r)}{1+2\hat{V}(r)} \cdot \frac{1+2\hat{V}(\tilde{r})}{1-2\hat{V}(\tilde{r})}. \tag{21}$$

This condition is the core of our hyperboloidal method. It ensures that the outgoing characteristic speed is unchanged under the compactifying hyperboloidal transformation; see figure 1 (left) (grey curve overlapping black dotted curve), independent of the choice for Ω. We set Ω as follows:

$$\Omega(\tilde{r}) = 1 - f(\tilde{r}) \quad \text{with} \quad f(\tilde{r}) = \left(\frac{X}{w}\right)^k \Theta(X),\ X = \tilde{r} - \tilde{r}_{\mathrm{TR}}, \tag{22}$$

[4] One may object that for h' of (20) in the limit $\Omega \to 0$ $\frac{1+2n\cdot lV}{1-2n\cdot l^2V} < h'$. By expanding this inequality in Ω at 0, it becomes clear that this can only be if $LH < 0$.

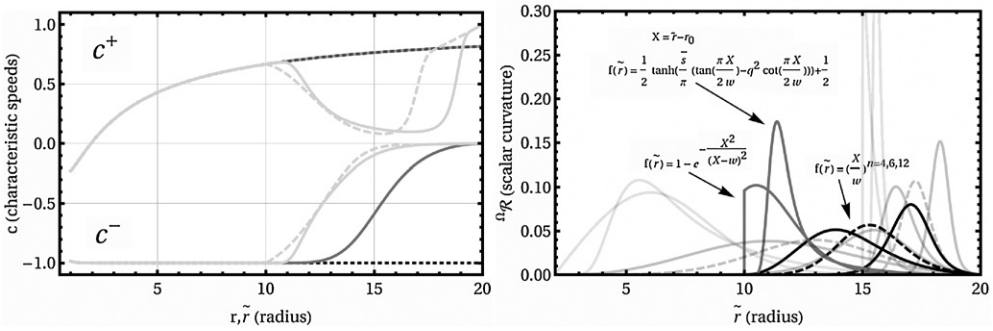

Figure 1. Left: characteristic speeds $c^{\pm}$ of the systems (8) and (9) for Kerr $a = 0.5$ on t-slices (black dotted curve) $r \in [2; 20]$ and compactified hyperboloidal $\tilde{t}$-slices with $\tilde{r}|_{\mathscr{J}^+} = 20$ attached at $r_{\mathrm{TR}} = 10$ for the hyperboloidal matching condition (21) (grey curve) and for (23) with $C = 20$ of [1, 5, 6, 8] (light-grey curve) for transition functions f–tanh–tan (light-grey solid curve) with $q = 1, \tilde{s} = 2$ [5, 8] and f-exp (light-grey dashed curve) [1, 6]. Right: $^{\Omega}\mathcal{R}(\tilde{r})$ for the conformal factors (transition functions $f(\tilde{r})$) of [1, 5, 6, 8] (grey curve) and our choice ($k = 6$, black dashed curve). The same five curves are shown in two light-grey groups for shifted transition points $r_{\mathrm{TR}} = 2; 15$.

where $\tilde{r}_{\mathrm{TR}}$ is the transition point and w is the width of the hyperboloidal domain.

In the original work [1] and also adapted from [5, 6, 8], the height-function derivative was set to

$$h' = f\, H_{\mathrm{ext}} = f\left(1 + \frac{4M}{r} + \frac{(8M^2 - C^2)}{r^2}\right) \tag{23}$$

where C is a parameter and f ranging from 0 to 1 is a transition function and the conformal factor was set to $\Omega(\tilde{r}) = 1 - f(\tilde{r})\frac{\tilde{r}}{\tilde{s}}$, $S = \tilde{r}|_{\mathscr{J}^+}$. H_{EXT} has the correct asymptotic singular behaviour, where $c^+|_{\mathscr{J}^+} = S^2/C^2$, but the characteristic speed in the hyperboloidal domain is left uncontrolled in the transition zone and depends on the details of f (as the spacelike condition (13)). In this case, $c^{(\tilde{k})}$, see equation (18), drops like Ω^2 before h' in the denominator sets in to result in a nonzero $c^{(\tilde{k})}$ asymptotically. This effect is apparent in figure 1 (left) (light-grey and light-grey dashed curves), where we plotted $c^{\pm}$ (14) for our choices (20) and (21) and for (23) as in [1, 5, 6, 8].

4. Wave equation on hyperboloidal slicing

In the following, we derive the explicit expressions for $^{\Omega}\tilde{g}^{\mu\nu}$, $^{\Omega}\mathcal{R}$ and $\Gamma^{\mu}(^{\Omega}\tilde{g})$ that appear in the conformal wave equation (6) under the compactifying conformal hyperboloidal transformations (11)–(13). We identify all formally singular terms, which could constitute potential obstacles for numerical evaluations at the outer boundary $\mathscr{J}^+$.

4.1. Transformation of the Kerr–Schild metric $g^{\mu\nu}$ and $\mathcal{R}$, Γ^{μ}

The metric components $g^{0\mu}$, g^{ij} and the determinant of $g^{\mu\nu}$ transform in a straightforward manner and divergent terms cancel trivially; the expressions are given in appendix A. The regularity of

$$^{\Omega}\tilde{g}^{00} = (1 - 2n \cdot l^2 V)\left(\frac{h' - K_+}{\Omega^2}\right)(h' - K_-), \qquad K_{\pm} = \frac{\pm I + 2n \cdot lV}{1 - 2n \cdot l^2 V} \tag{24}$$

at $\mathscr{I}^+$ is guaranteed by the form of h' in equation (20), since $\frac{1-2M/r}{1+2M/r}K_+ =: 1 + \frac{1}{r^2}G \overset{r\to\infty}{\longrightarrow} 1$ in asymptotically flat spacetimes[5] and we obtain

$$ {}^{\Omega}\tilde{g}^{00} = (1 - 2n\cdot l^2 V)\frac{1+2M/r}{1-2M/r}\left(-HL - \frac{1}{\tilde{r}^2}G\right)(h' - K_-). \tag{25}$$

The scalar curvature ${}^{\Omega}\mathcal{R}$ of ${}^{\Omega}g^{\mu\nu}$ is given by

$$ {}^{\Omega}\mathcal{R} = -\frac{6}{\tilde{r}}((1 - 2n\cdot l^2 V)N + \dot{\Omega}L(3 - 2V) - \dot{\Omega}L\tilde{r}\,{}^{\Omega}\gamma\, n\cdot l), \tag{26}$$

$$ {}^{\Omega}\mathcal{R} = -\frac{6}{\tilde{r}}((1 - 2n\cdot l^2 V)N + \dot{\Omega}L(3 - 4V)) \text{ for Kerr}, \tag{27}$$

$$ N := \frac{1}{\Omega^2}(\Omega'' r - \Omega') = (\ddot{\Omega}\Omega^2\tilde{r}L - \dot{\Omega}(\Omega - 3\dot{\Omega}\tilde{r}))L^2, $$

where ${}^{\Omega}\gamma := \gamma/\Omega$ depends on the Kerr–Schild metric in question. In Kerr, $\gamma = 2M/s$; compare with (7). In certain cases, it is useful to distinguish the conformal factor Φ and the rescaling factor Ω, and then $\mathcal{R}$ changes as in appendix B. Besides h', the conformal factor has to be picked carefully to avoid steep gradients in ${}^{\Omega}\tilde{g}^{\mu\nu}$ and ${}^{\Omega}\mathcal{R}$ (which appear on the rhs of equations (8) and (9)) as shown in figure 1 (right).

Next, we derive the expressions for $\Gamma^{\mu}({}^{\Omega}\tilde{g})$, where we first consider the conformal transformation behaviour of $\Gamma^{\mu}(g)$ under equation (12):

$$ \Gamma^{\mu}({}^{\Omega}g) = {}^{\Omega}\Gamma^{\mu}(g) + {}^{\Omega}C^{\mu}, \tag{28}$$
$$ {}^{\Omega}C^{\mu} = -2\dot{\Omega}L({}^{\Omega}n^{\mu} - 2\,n\cdot l\,{}^{\Omega}V\,l^{\mu}), $$

where ${}^{\Omega}C^{\mu}$ is a tensor, ${}^{\Omega}\Gamma^{\mu}(g) = \Gamma^{\mu}(g)/\Omega^2$, ${}^{\Omega}n^{\mu} = (0, n^i)/\Omega$ and ${}^{\Omega}V = V/\Omega$.

The transformation of $\Gamma^{\mu}({}^{\Omega}g)$ to compactified hyperboloidal coordinates involves the Hessian of (11) and (13). We obtain

$$ \Gamma^{\mu}({}^{\Omega}\tilde{g}) = \tilde{\Gamma}^{\mu}({}^{\Omega}g) - \frac{\partial\tilde{x}^{\mu}}{\partial x^{\nu}\partial x^{\lambda}}\,{}^{\Omega}g^{\nu\lambda} \tag{29}$$

$$ \frac{\partial\tilde{x}^{\mu}}{\partial x^{\nu}\partial x^{\lambda}}\,{}^{\Omega}g^{\nu\lambda} = \frac{1}{\Omega^2}\left\{-h''(1 - 2n\cdot l^2 V) + 2h'\frac{1}{r}V(1 - n\cdot l^2) - 2h'\frac{1}{r}, \right. \tag{30}$$
$$ \left. n^i\left((\Omega'' r - \Omega')(1 - 2n\cdot l^2 V) + \Omega'(5 - 2V)\right) - 4l^i\,\Omega' n\cdot l V\right\} $$

$$ \frac{\partial\tilde{x}^{\mu}}{\partial x^{\nu}\partial x^{\lambda}}\,{}^{\Omega}g^{\nu\lambda} = \left\{-L\frac{d}{d\tilde{r}}h'(1 - 2n\cdot l^2 V) + 2h'\frac{1}{\tilde{r}}{}^{\Omega}V(1 - n\cdot l^2) - 2h'\frac{1}{\Omega\tilde{r}}, \right. \tag{31}$$
$$ \left. n^i(N(1 - 2n\cdot l^2 V) + \dot{\Omega}L(5 - 2V)) - 4l^i\dot{\Omega}L\,n\cdot l V\right\}. $$

A closer look at the time component $\Gamma^0({}^{\Omega}\tilde{g})$ reveals that the third term in equation (31) is divergent. It cancels with $-2\dot{\Omega}L\,{}^{\Omega}\tilde{n}^0 = -2\dot{\Omega}L(-h'/\Omega)$ that appears through the coordinate transformation ${}^{\Omega}C^{\mu} \to {}^{\Omega}\tilde{C}^{\mu}$; see equation (28). We remove these terms from ${}^{\Omega}H^{\mu} := \frac{\partial\tilde{x}^{\mu}}{\partial x^{\nu}\partial x^{\lambda}}\,{}^{\Omega}g^{\nu\lambda}$ and ${}^{\Omega}\tilde{C}^{\mu}$ and denote them as ${}^{\Omega}H^{\mu}_{\mathrm{R}}$ and ${}^{\Omega}\tilde{C}^{\mu}_{\mathrm{R}}$, where ${}^{\Omega}D^{\mu}$ is the remainder of the cancellation:

$$ \Gamma^{\mu}({}^{\Omega}\tilde{g}) = {}^{\Omega}\tilde{\Gamma}^{\mu}(g) + {}^{\Omega}\tilde{C}^{\mu}_{\mathrm{R}} - {}^{\Omega}H^{\mu}_{\mathrm{R}} + {}^{\Omega}D^{\mu}, \tag{32}$$

$$ {}^{\Omega}D^{\mu} := \left\{2h'L\frac{1}{\tilde{r}}, 0, 0, 0\right\}. \tag{33}$$

[5] $\frac{1-2M/r}{1+2M/r}K_+ = 1 + \frac{4M}{r^2}(n\cdot l_1 + V_1) + \mathcal{O}(r^{-3})$, and in Kerr, $\frac{1-2M/r}{1+2M/r}K_+ = 1 - \frac{4M}{r^3}(a^2(n_z)^2) + \mathcal{O}(r^{-4})$.

5. Numerical applications

We are now ready for a numerical application of the methods described in the last section. We solve the system (9) using a (3+1) FD code on attached hyperboloidal slices using g as in equation (21) and h' as in equation (23) as most commonly used in the literature and compare the evolution of the numerical errors. Then, we solve the system (8) using a PS evolution scheme in (3+1), which allows higher accuracy than the FD code, to obtain new insights into the splitting of the late-time tails of the solution [6, 7] and confirm known results about polynomial decay rates at finite radii and $\mathscr{I}^+$. We also inspect the late-time part of the solution at the horizon, where oscillations have been predicted [16, 17] but until now not regarded in numerical studies.

With both implementations, we evolve non-stationary compactly supported initial data (ID) of the forms $\psi(0, x^i) = 0,\ \psi_j(0, x^i) = 0$ and

$$\psi_0(0, \tilde{x}^i) = Y^{l_0 m}(\tilde{x}^i)\, \mathrm{e}^{-(\tilde{r}-\tilde{r}_0)^2/(2\sigma^2)} \tag{34}$$

and of the form

$$\psi_0(0, \tilde{x}^i) = \mathrm{e}^{-(\tilde{x}^i-\tilde{x}^i_0)(\tilde{x}^j-\tilde{x}^j_0)\delta_{ij}/(2\sigma^2)}, \tag{35}$$

where $\sigma, \tilde{r}_0$ and $\tilde{x}^i_0$ are the parameters and $Y^{l_0 m}(\tilde{x}^i)$ are the spherical harmonics w.r.t. $\tilde{x}^i$. We set the Kerr parameter $M = 1$ and define the local power index (LPI) to be $\mathrm{LPI}([\psi]^{lm}) := \mathrm{d}\log|[\psi]^{lm}|/\mathrm{d}\log t$, where $[\psi]^{lm}$ is the lm-spherical harmonic component of the field w.r.t. Kerr–Schild coordinates.

5.1. FD code

Our FD code is embedded in the Cactus parallelization framework [18]. We made use of the extension Llama [19] of the Carpet driver [20], which handles the domain decomposition of grids over processors and provides the required interpolation operations for boundary communication. The Llama code, comparable to the multiblock code of [21], allows us to use a spherical grid with the 'inflated cube' coordinates [22] in the angular directions, which consists of six overlapping coordinate patches each with two angular coordinates of the general form $\rho = \arctan(x^i/x^k)$, $i \neq k$. The finite differences are computed of ${}^{\Omega}\psi_0$ and ${}^{\Omega}\tilde{F}^i$ in the radial and angular coordinates, and then transformed into a common Cartesian basis and input to the rhs of equation (9). The discretization of the fluxes ${}^{\Omega}\tilde{F}^i$ instead of the evolution variables ψ_i is beneficial for a long-term stable evolution. If used on a single Cartesian grid, see, e.g., [23] and references therein, the form of equation (9) is a necessary condition for the FD scheme to conserve a certain discrete energy norm [24]. Since we compute non-Cartesian FDs and use multiple overlapping coordinate patches, we require additional Kreiss–Oliger-type artificial dissipation [25] to guarantee the long-term stability. We use the MoL with the fourth-order Runge–Kutta time integration, sixth-order FD operators and add fifth-order artificial dissipation[6] (except at the radial boundaries) to the rhs of the evolution equation for ψ_0.

5.1.1. FD code: comparison of matching methods. As a non-trivial test case, we evolved off-centred Gaussian ID with $\tilde{x}^i_0 = (2.4, 1.2, 1.1)$, $\sigma = 1$ on the dented $\tilde{t}$-slicing, see equation (23), corresponding to the solid light-grey curve in figure 1 (left) and on the smoother $\tilde{t}$-slicing, see equation (21), corresponding to grey curve in figure 1 (left). We set the radial

[6] This is different from the six-patch code of [21], where summation-by-parts FD and dissipation operations are used at grid and patch boundaries.

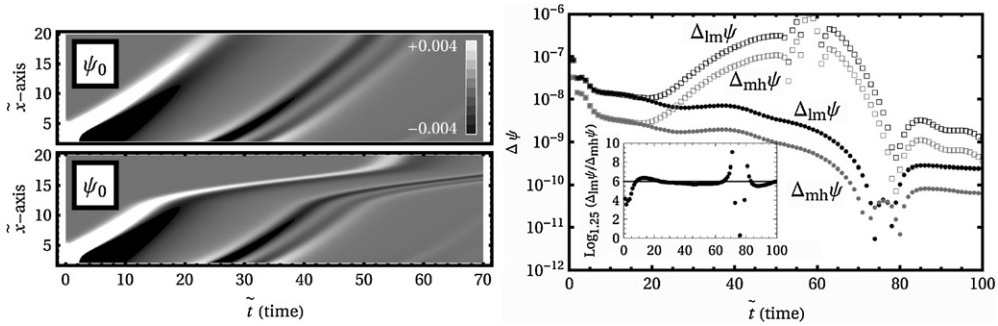

Figure 2. Left: evolution of ψ_0 along the $\tilde{x}$-axis for off-centred ID on dented hyperboloidal slicing (bottom) and smooth slicing (top) for Kerr $a = 0.1$. Slicing parameters and characteristic speeds as in figure1 (left): light-grey curve (f-tanh-tan) and grey curve (equation (21)). The outgoing characteristic speed c^+ drops in the hyperboloidal domain, which is apparent in the solution. Right: evolution of the errors of ψ along the $\tilde{x}$-axis for $l_0 = 0$ ID on dented slicing (squares) and smooth slicing (dots) for three resolutions $\Delta_{l,m,h}\tilde{r} = 0.0625, 0.05, 0.04$ with fixed $N_\rho = 41$. Inset: convergence rate on smooth slicing.

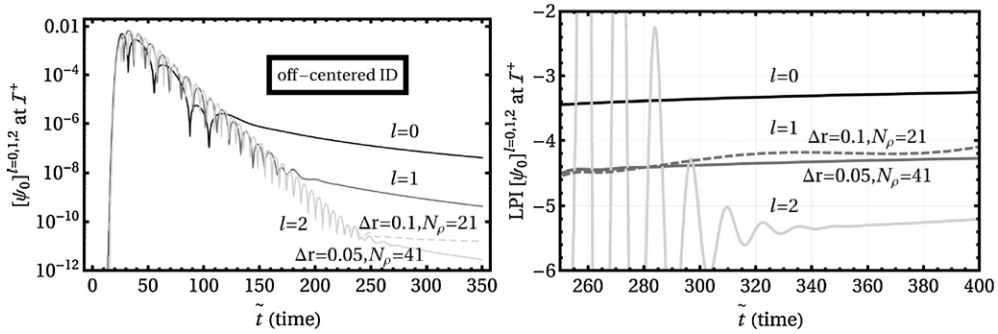

Figure 3. Evolution of the components $[\Psi_0]^{l=0,2,4}$ at $\mathscr{I}^+$ for off-centred ID on smooth hyperboloidal slicing. Setup as in figure 2 (left top). The field components decay at late times with a power law $\sim \tilde{t}^{-n}$ as apparent in the right plot. Sufficiently high resolution is necessary to see the correct power law at low amplitudes (dashed curves).

grid spacing to $\Delta\tilde{r} = 0.05$, the time step to $\Delta\tilde{t} = 0.04$ and the number of angular grid points per patch to $N_\sigma \times N_\rho = 41 \times 41$.

In figure 2, the outward propagation of the initial Gaussian pulse along the $\tilde{x}$-axis is shown. The pulse passes the transition point $r_{\mathrm{TR}} = 10$ on the smooth slicing without apparent interferences (top panel). On the dented slicing (lower panel), the pulse slows down in agreement with c^+ of figure 1 (light grey) and leaves the numerical domain at later time. The larger gradients in the field at a given time, due to the bump in c^+, cause the numerical error to be bigger as shown in figure 2 (right).

The decomposition of the field ψ_0 at $\mathscr{I}^+$ into spherical harmonics is shown in figure 3, an exponential oscillatory decay, followed by a polynomial decay with the asymptotic behaviour $\sim \tilde{t}^{-n}$ in agreement with the rule $n = l + 2$ for ψ, i.e. $n = l + 3$ for ψ_0, derived analytically in [26] and confirmed in the recent numerical studies [6, 7]. We go into more detail about asymptotic decay rates in the next section, where we use PS methods and quad machine precision.

5.2. Spectral code

To resolve the late-time part of the solution, higher numerical accuracy and machine precision are required than those we are able to obtain with the FD implementation described in the last section; see figure 3. For this reason, we created a code that uses spectral methods to compute spatial derivatives and the MoL with the fourth-order Runge–Kutta time integration. In the spectral domain, the evolution variables are expanded into real spherical harmonics Y^{lm} (angular direction) and Chebyshev polynomials C^n (radial direction), i.e. into the basis of polynomials $P^{lmn} := Y^{lm}\,C^n$, where we use Gauss–Legendre and Gauss–Lobatto collocation points, respectively. The hyperboloidal method in combination with horizon penetrating coordinates does not require any boundary treatment and unlike the FD implementation we use hyperboloidal slices that cover the whole numerical grid, i.e. beginning at the first and ending at the last collocation point, where we use as for the FD code the polynomial conformal factor (22) with $k = 6$, which is exactly represented in the coefficients space. If we wanted to use a hyperboloidal domain that covers the grid only partially, we would require two spectral domains that are joined at the transition point r_{TR}, since the piecewise function Ω (22) defined on a single spectral domain contains the Heaviside function which is badly represented in the coefficients space.

The spherical harmonics and their derivatives Y^{lm}, $\partial_j Y^{lm}$ are expressed in the Cartesian coordinates, similar to SpEC; see, e.g., [27]. They are evaluated through another basis of harmonics $\Phi^{lm} = (n^j \mathcal{N}_j^{[lm]})^l$, where $\mathcal{N}_j^{[lm]}$ are constant complex null vectors $\mathcal{N}_i \mathcal{N}_j \delta^{ij} = 0$ labelled by l and m, spanning the $2l + 1$ harmonics in each l-eigenspace. We chose the same $\mathcal{N}_j^{[lm]}$ as in [28], such that Y^{lm} and Φ^{lm} are related by a Fourier transform in each l-eigenspace:

$$Y^{lm} = B^{lm} \sum_{m'=-l}^{l} \Phi^{lm'} \mathrm{e}^{-i\,m'm\,a_l}, \qquad B^{lm} = (-1)^m \frac{1}{l!} \sqrt{\frac{(l+m)!(l-m)!}{4\pi\,(2l+1)}}, \tag{36}$$

where $a_l = 2\pi/(2l+1)$. The derivatives $\partial_j \Phi^{lm}$ take the simple form

$$\partial_j \Phi^{lm} = \partial_j n^i \left(n^k \mathcal{N}_k^{[lm]}\right)^{l-1} l\, \mathcal{N}_j^{[lm]}, \tag{37}$$

where $\partial_j n^i = (\delta^{ij} - n^i n^j)/r$ and, thus, are tangential to the unit sphere. Given the decomposition of a function ψ into the polynomial basis P^{lmn}, we obtain the tangential component of the derivative ${}^{\parallel}(\partial_j)\psi$ through $\partial_j Y^{lm}\,C^n$ and the radial component $\partial_r \psi$ through $Y^{lm} \partial_r C^n$ (or alternatively, through a recurrence relation for the Chebyshev coefficients). The complete partial derivative of ψ is then given by

$$\partial_j \psi = n_j\, \partial_r \psi + {}^{\parallel}(\partial_j)\psi. \tag{38}$$

Since we compute the rhs of equation (8) in the physical space, we introduce an aliasing error, which would cause high modes $> l_{\mathrm{MAX}}$ to blow up during the evolution. For our implementation, it was enough to erase the l_{MAX} components of the rhs of ψ and ψ_0 at every step of the time integration to obtain a stable long-term evolution and to leave the rhs of ψ_j untouched.

5.2.1. Spectral code: application to late-time decay rates in Kerr. A generic non-stationary compactly supported perturbation on the Schwarzschild background decays at late times as $t^{-n}, n = 2l + 3$ [29]. On the Kerr background, the picture is more complicated. Since Kerr is not spherically symmetric, neighbouring l-modes are coupled. Until recently there was a controversy in the literature about the value of n for $l \geqslant 4$. In the simple picture, the lowest l-mode (compatible with the azimuthal and equatorial symmetries of the ID) generated by mode mixing during the evolution is

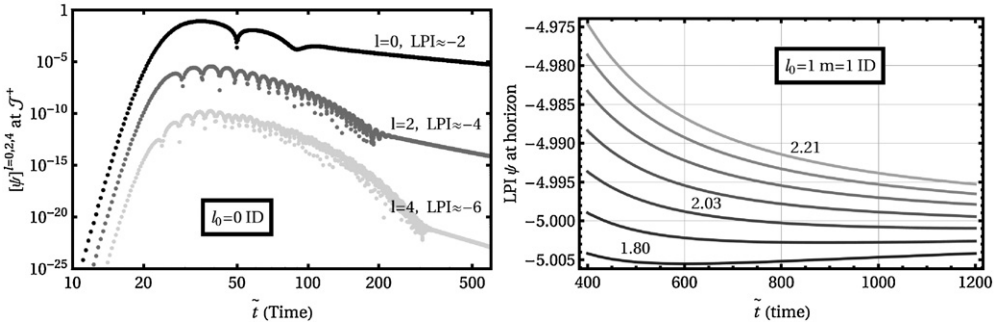

Figure 4. Left: field components $[\psi]^{l=0,2,4}$ at $\mathscr{J}^+$ for l_0 ID in Kerr $a = 0.5$. The decay rates are in agreement with the rule $n = l + 2$. Right: LPI of ψ around the horizon between $\tilde{x}^i = (1.8 - 2.21, 0, 0)$ for $(l_0 = 1, m = 1)$ ID in Kerr $a = 0.1$ with $N_r = 90$, $N_\theta = 6$ grid points. The asymptotic decay rates approach $n = 5$ in agreement with $n = l_0 + l + 3$.

dominating the solution at late times. Nevertheless, analytical work by Barack and Ori [16] and Hod [26] predict a surprising dependence of n (memory effect) on the initially excited mode l_0, i.e. $n = n(l, l_0)$. By several numerical studies [27, 30–32], it was justified that both pictures are correct and that the decay rate depends on the details of the initial value formulation, i.e. the particular coordinates (Kerr–Schild and Boyer–Lindquist) in which the spherical harmonics are defined and the particular choice of ID. Therefore, we distinguish between BL harmonics l_{BL} and KS harmonics l_{KS} in the following through subscripts, where necessary. Another effect that was predicted by Barack and Ori [16, 17] is oscillations on the late-time solution at the horizon (OAH).

Recently, the use of hyperboloidal slices in Kerr allowed Zenginoğlu and Tiglio [6] to extend this numerical investigation of polynomial decay rates at finite radii to future null infinity (compactly supported non-stationary ID $l_0 < 5$). Very recently, Racz and Toth [7] presented a more detailed study for various kinds of ID, including different fall-off properties towards null infinity up to $l_0 < 6$, where they investigated the behaviour of the sub-dominant modes as well (l-modes with decay faster than the slowest decaying mode). They could confirm numerically the m-independent rule, $n = l_0 + l + 3$ for $l \geqslant l_0$ and $n = l_0 + l + 1$ for $l < l_0$ proposed earlier by numerical studies [31, 32], which covers the formulae derived analytically in [16, 26]. For the late-time tails at $\mathscr{J}^+$ (TAS), the results of [6, 7] were found to fit the rule $n = l + 2$ for $l \geqslant l_0$ and $n = l_0$ for $l \leqslant l_0 - 2$, which has been obtained analytically in [26]. The authors of [7, 6] found a radial splitting of the decay rates for certain values of l_0, l and m, where the decay exponent varies for observers near the black hole, distant observers and at $\mathscr{J}^+$. Moreover, the effect was found to depend on the harmonic index m [7]. We observe such a splitting in our simulations as well (SPL).

As an application of the hyperboloidal method, we investigated the effects OAH, TAS and SPL on the late-time tails in Kerr. At first we check the convergence of the code for the non-trivial test case of off-centred ID; see figure 6.

TAS: figure 4 (left) confirms that the late-time tail decay rates at $\mathscr{J}^+$ are in agreement with the rule $n = l + 2$, where the evolution of the $l = 0, 2, 4$ modes of ψ for $l_0 = 0$ ID is shown.

OAH: In figure 4 (right), we show the LPI of ψ in the neighbourhood of the horizon for $\tilde{r} = 1.8 - -2.2$. The field decays in agreement with the rule $n = l_0 + l + 3$ but no oscillations

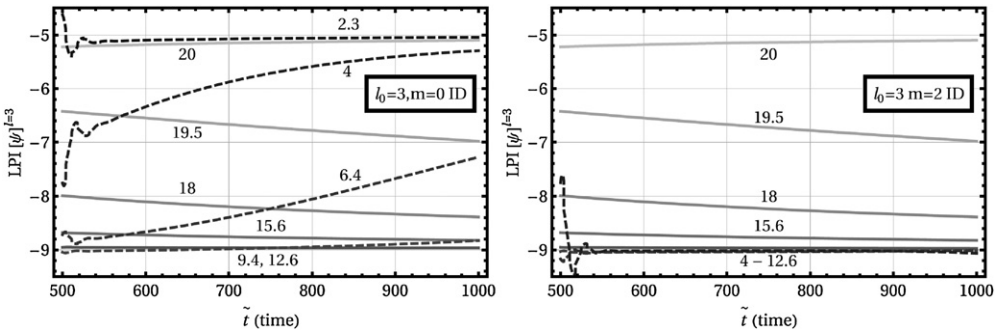

Figure 5. LPIs of $[\psi]^{l=3\,m=0}$ (left) and $[\psi]^{l=3\,m=2}$ (right) for $(l_0 = 3, m = 0, 2)$ ID at radii between $r = 2--12$ (dashed lines) and $r = 12--20$ (solid lines). The splitting, (see the text) of the LPIs at different radii for $m = 0$ is shown compared to $m = 2$, where no splitting appears. For $N_r = 90$, $N_\theta = 7$ grid points and $a = 0.05$.

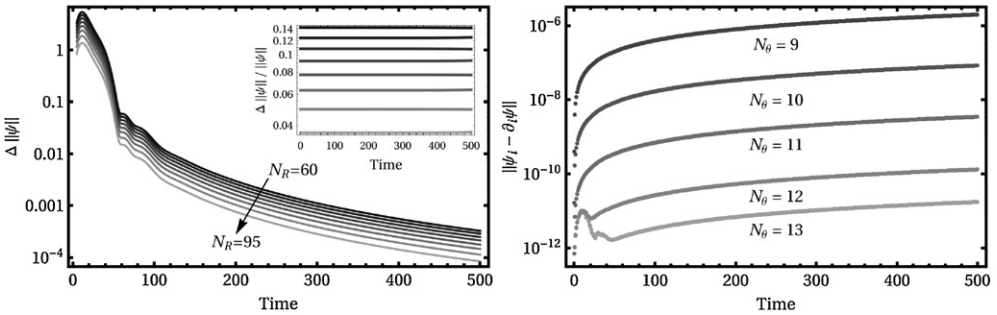

Figure 6. Left: convergence of L_2-norm of $\Delta\psi$ for off-centred ID with $N_r = 60, 65, 70, 75, 80, 85, 90, 95$, where $\Delta\psi$ is computed w.r.t. $N_r = 110$. $a = 0.9$, $N_\theta = 10$and $\Delta t = 0.1$ are fixed. Right: convergence of constraint field $\psi_i - \partial_i\psi$ at $N_\theta = 13, 12, 11, 10, 9$ with fixed $a = 0.9$, $N_r = 65$and $\Delta t = 0.1$.

are present. The reason is the co-rotating azimuthal coordinate[7] $\phi_+ = \phi_{\rm BL} - t_{\rm BL}\Omega_+$ used in [16, 17], where the Kerr–Schild $\phi_{\rm KS} = \arctan y/x$ as $\tilde{\phi}$, which was used in [33], is independent of $t_{\rm BL}$.

SPL: As we can see in figure 5 (left), the LPI of $[\psi]^{l=3,m=0}$ for $(l_0 = 3, m = 0)$ ID varies between $n = 5$ for $2 < \tilde{r} < 12$ (dashed lines), $n = 9$ for $12 < \tilde{r} < 20$ (solid lines) and $n = 5$ for $\tilde{r} = 20$ at $\mathscr{I}^+$. We observed the same splitting for $(l_0 = 3, m = 1)$ ID (not shown). This effect is not present for $(l_0 = 3, m = 2)$ ID as shown in figure 5 (right) and for $(l_0 = 3, m = 3)$ ID (not shown). The reason is that the Kerr–Schild $(l_0 = 3, m = 0, 1)$ ID as well as the examined l mode contain the $l_{\rm BL} = 1$ harmonic, which decays with $n = 1 + 1 + 3$. The ratio of the $l_{\rm BL} = 1$ harmonic in the $l = 3$ Kerr–Schild mode decreases in the limits $a \to 0$ and $r \to \infty$, where we observe the field decaying with $n = 3 + 3 + 3$. It vanishes at $\mathscr{I}^+$, where the BL and KS inclination coordinates agree and there the field decays like $n = 3 + 2$. By setting $m > 1$, we can exclude $l_{\rm BL} = 1$ from the ID and the splitting vanishes.

[7] According to [16, 17], the field decays at late times, like $\sim t^{-n}\,\mathrm{e}^{\mathrm{i}m\Omega_+ v(t,x^i)}$, where $v \sim t$ is the Eddington–Finkelstein null coordinate and $\Omega_+ = a/(2Mr_+)$, $r_+ = M + (M^2 - a^2)^{1/2}$.

6. Conclusions

We applied a compactifying conformal hyperboloidal (cch) transformation to the wave operator of Kerr–Schild metrics and derived all expressions, and removed formally singular terms of the conformal wave equation for which the numerical evaluation at the outer boundary might be problematic. The hyperboloidal slices we used in that process let the outgoing characteristic speed invariant under the cch transformation independent of the Kerr–Schild metric in question. This was possible by analysing the characteristic speeds of the first-order reduced wave equation, whereby we obtained access to the arbitrary part H of the height-function derivative for which the constraints on h' are automatically satisfied (suitable asymptotic behaviour, spacelike condition). This part allows us to directly set the outgoing characteristic speed to the desired function of radius in the hyperboloidal domain equation (21) and thereby to get more control on the efficiency and accuracy of the hyperboloidal method in numerical calculations, which we demonstrated through comparison with existing approaches in the literature. As an application, we have numerically verified the known decay rates of scalar test fields and their sub-dominant modes in Kerr at the horizon, finite radii and at $\mathscr{I}^+$ and obtained new insights into the m-dependence of the radial splitting of the late-time decay rates of certain harmonic modes.

The asymptotics of hyperboloidal slices simplify the boundary treatment in numerical simulations and provide a clean solution to the wave extraction problem. Moreover, the cch coordinate transformation beyond the boundary can act like an adaptive numerical grid on the background, i.e. H and Ω can be used to uniformly spread grid points or act as a magnifier to increase the spatial or temporal resolution, say in the neighbourhood of a localized source. In addition to providing that, the expressions presented here could lead to applications of the hyperboloidal approach to Kerr–Schild metrics beyond Kerr. The next step in improving the PS code would be to implement two spectral domains to be able to use piecewise-defined conformal factors. It would be interesting to test the stability of the FD and PS code with nonlinear source terms as in [5] or to use a localized moving effective source [8] to compute the scalar self-force on a particle orbiting a Kerr black hole and finally to extend the code to handle gravitational perturbations on Kerr–Schild backgrounds.

Acknowledgments

It is a pleasure to thank Badri Krishnan, Anıl Zenginoğlu, Frank Ohme, Barry Wardell, Alex B. Nielsen, José Luis Jaramillo, Gaurav Khanna and Leor Barack for useful discussions. I am grateful for advice from Ian Hinder and Daniela Alic on the long-term stability of FD codes and from Nico Budewitz for technical support on the computer cluster at the AEI. I also thank the many developers of the Cactus, Carpet and the Llama codes and the very useful SimFactor. This work was supported by the IMPRS for Gravitational Wave Astronomy in the MPS. The preprint number for the Albert Einstein Institute is AEI-2011-095.

Appendix A. Metric components ${}^{\Omega}\tilde{g}^{ij}$, ${}^{\Omega}\tilde{g}^{0j}$ and $\det {}^{\Omega}\tilde{g}_{\mu\nu}$

The cch transformations (11)–(13) change the metric components g^{0j} and g^{ij} of equation (1) to

$$ {}^{\Omega}\tilde{g}^{0j} = {}^{\Omega}\tilde{\eta}^{0j} - 2^{\Omega}V\,\tilde{l}^{0\Omega}\tilde{l}^{j}, \qquad {}^{\Omega}\tilde{g}^{ij} = {}^{\Omega}\tilde{\delta}^{ij} - 2V^{\Omega}\tilde{l}^{i\Omega}\tilde{l}^{j}, \tag{A.1} $$

$$ {}^{\Omega}\eta^{0j} = -h'Ln^{j}, \qquad {}^{\Omega}\delta^{ij} = \delta^{ij} + \tilde{r}\dot{\Omega}L(2+\tilde{r}\dot{\Omega}L)\,n^{i}n^{j}, \tag{A.2} $$

$$\tilde{l}^0 = l^0 - h' n \cdot l, \qquad {}^{\Omega}\tilde{l}^i = l^i + n^i \tilde{r}\dot{\Omega} L\, n \cdot l, \tag{A.3}$$

where ${}^{\Omega}V = V/\Omega$, in Kerr ${}^{\Omega}V = {}^{\Omega}r_{\rm BL}/{}^{\Omega}s$ with ${}^{\Omega}s(\tilde{r},\tilde{z}) = \Omega^2 s(\tilde{r},\tilde{z}) = \sqrt{(\tilde{r}^2 - (\Omega a)^2)^2 + (2a\Omega\tilde{z})^2}$ and ${}^{\Omega}r_{\rm BL} = \frac{1}{\sqrt{2}}\sqrt{\tilde{r}^2 - \Omega^2 a^2 + {}^{\Omega}s}$. The determinant is

$$\det g_{\mu\nu} = 1 \quad \rightarrow \quad \det {}^{\Omega}\tilde{g}_{\mu\nu} = 1/L^2. \tag{A.4}$$

Appendix B. ${}^{\Phi}\mathcal{R}$ for $\Phi \neq \Omega$

In certain cases, it can be useful to distinguish the conformal factor $\Phi = \Omega\lambda$ and the radial rescaling factor Ω, i.e. $\lambda \neq 1$, say if the metric should be left unchanged but the numerical grid has to be adapted in some region. In that case, ${}^{\Omega}g^{\mu\nu} \rightarrow {}^{\Omega\lambda}g^{\mu\nu}$ in equation (9) and ${}^{\Phi}\mathcal{R}$ becomes

$${}^{\Phi}\mathcal{R} = -\frac{6}{\lambda^3}\left[\frac{1}{\tilde{r}}((1 - 2n\cdot l^2 V)\hat{N} + L\dot{\Phi}(3 - 2V)) - L\dot{\Phi} n \cdot l\, {}^{\Omega}\gamma\right], \tag{B.1}$$

$${}^{\Phi}\mathcal{R} = -\frac{6}{\lambda^3\tilde{r}}[(1 - 2n\cdot l^2 V)\hat{N} + L\dot{\Phi}(3 - 4V)] \quad \text{inKerr}, \tag{B.2}$$

where $\hat{N} := \frac{1}{\Omega^2}(\Phi'' r - \Phi') = L^2(L_1\dot{\Phi} + \Omega\ddot{\Phi})\tilde{r} - L\dot{\Phi}$, $L_1 := 2\dot{\Omega} + \ddot{\Omega}\Omega\tilde{r}L$. The conformal transformation $\Gamma^{\mu}({}^{\Omega}\tilde{g}) \rightarrow \Gamma^{\mu}({}^{\Omega\lambda}\tilde{g})$ of equation (32) is given by

$$\Gamma^{\mu}({}^{\Omega\lambda}\tilde{g}) = {}^{\Omega}\tilde{\Gamma}^{\mu}(g)/\lambda^2 + {}^{\Omega\lambda}\tilde{C}^{\mu}_{\rm R} - {}^{\Omega}H^{\mu}_{\rm R}/\lambda^2 + {}^{\Omega\lambda}D^{\mu}, \tag{B.3}$$

$${}^{\Omega\lambda}C^{\mu} = -2\dot{\Phi}L({}^{\Omega\lambda}n^{\mu} - 2\, n\cdot l\, {}^{\Omega\lambda}V\, l^{\mu})/\lambda^2, \tag{B.4}$$

$${}^{\Omega\lambda}D^{\mu} = \left\{2h'L\frac{1}{\tilde{r}}\left(\tilde{r}\dot{\lambda}/\lambda + 1\right), 0, 0, 0\right\}/\lambda^2. \tag{B.5}$$

References

[1] Zenginoğlu A 2008 Hyperboloidal foliations and scri-fixing *Class. Quantum Grav.* **25** 145002
[2] Zenginoğlu A 2008 A hyperboloidal study of tail decay rates for scalar and Yang–Mills fields *Class. Quantum Grav.* **25** 175013
[3] Zenginoğlu A, Nunez D and Husa S 2009 Gravitational perturbations of Schwarzschild spacetime at null infinity and the hyperboloidal initial value problem *Class. Quantum Grav.* **26** 035009
[4] Friedrich H 1983 Cauchy problems for the conformal vacuum field equations in general relativity *Commun. Math. Phys.* **91** 445–72
[5] Zenginoğlu A and Kidder L E 2010 Hyperboloidal evolution of test fields in three spatial dimensions *Phys. Rev.* D **81** 124010
[6] Zenginoğlu A and Tiglio M 2009 Spacelike matching to null infinity *Phys. Rev.* D **80** 024044
[7] Racz I and Toth G Z 2011 Numerical investigation of the late-time Kerr tails *Class. Quantum Grav.* **28** 195003
[8] Vega I, Wardell B and Diener P 2011 Effective source approach to self-force calculations *Class. Quantum Grav.* **28** 134010
[9] Bernuzzi S, Nagar A and Zenginoglu A 2011 Binary black hole coalescence in the large-mass-ratio limit: the hyperboloidal layer method and waveforms at null infinity *Phys. Rev.* D **84** 084026
[10] Zenginoğlu A and Khanna G 2011 Null infinity waveforms from extreme-mass-ratio inspirals in Kerr spacetime arXiv:1108.1816
[11] Zenginoğlu A 2011 A geometric framework for black hole perturbations *Phys. Rev.* D **83** 127502
[12] Rinne O 2010 An Axisymmetric evolution code for the Einstein equations on hyperboloidal slices *Class. Quantum Grav.* **27** 035014

[13] Chirenti C and Saa A 2011 Nonstationary regime for quasinormal modes of the charged Vaidya metric *Phys. Rev.* D **84** 064006
[14] Wald R M 1984 *General Relativity Book* (Chicago, IL: University of Chicago Press)
[15] Zenginoğlu A 2010 Asymptotics of black hole perturbations *Class. Quantum Grav.* **27** 045015
[16] Barack L and Ori A 1999 Late time decay of scalar perturbations outside rotating black holes *Phys. Rev. Lett.* **82** 4388
[17] Barack L and Ori A 1999 Late time decay of gravitational and electromagnetic perturbations along the event horizon *Phys. Rev.* D **60** 124005
[18] Goodale T, Allen G, Lanfermann G, Massó J, Radke T, Seidel E and Shalf J 2003 The Cactus framework and toolkit: design and applications *Vector and Parallel Processing—VECPAR'2002, 5th Int. Conf. (Lecture Notes in Computer Science)* (Berlin: Springer)
[19] Pollney D, Reisswig C, Schnetter E, Dorband N and Diener P 2011 High accuracy binary black hole simulations with an extended wave zone *Phys. Rev.* D **83** 044045
[20] Schnetter E, Hawley S H and Hawke I 2004 Evolutions in 3D numerical relativity using fixed mesh refinement *Class. Quantum Grav.* **21** 1465–88
[21] Schnetter E, Diener P, Dorband E N and Tiglio M 2006 A multi-block infrastructure for three-dimensional time-dependent numerical relativity *Class. Quantum Grav.* **23** S553–78
[22] Thornburg J 2004 Black hole excision with multiple grid patches *Class. Quantum Grav.* **21** 3665–92
[23] Calabrese G and Neilsen D 2004 Spherical excision for moving black holes and summation by parts for axisymmetric systems *Phys. Rev.* D **69** 044020
[24] Gustafsson B, Kreiss H O and Oliger J 1995 *Time Dependent Problems and Difference Methods* vol. 24 (New York: Wiley-Interscience)
[25] Kreiss H and Oliger J 1973 *Methods for the Approximate Solution of Time Dependent Problems* vol 10 (Geneva: Global Atmospheric Research Programme–WMO-ICSU Joint Organizing Committee)
[26] Hod S 2000 Mode coupling in rotating gravitational collapse of a scalar field *Phys. Rev.* D **61** 024033
[27] Scheel M A *et al* 2004 3-D simulations of linearized scalar fields in Kerr space-time *Phys. Rev.* D **69** 104006
[28] Jasiulek M 2009 A new method to compute quasi-local spin and other invariants on marginally trapped surfaces *Class. Quantum Grav.* **26** 245008
[29] Price R H 1972 Nonspherical perturbations of relativistic gravitational collapse: I. Scalar and gravitational perturbations *Phys. Rev.* D **5** 2419–2438
[30] Tiglio M, Kidder L E and Teukolsky S A 2008 High accuracy simulations of Kerr tails: coordinate dependence and higher multipoles *Class. Quantum Grav.* **25** 105022
[31] Burko L M and Khanna G 2011 Late-time Kerr tails: Generic and non-generic initial data sets, 'up' modes and superposition *Class. Quantum Grav.* **28** 025012
[32] Burko L M and Khanna G 2009 Late-time Kerr tails revisited *Class. Quantum Grav.* **26** 015014
[33] Krivan W, Laguna P and Papadopoulos P 1996 Dynamics of scalar fields in the background of rotating black holes *Phys. Rev.* D **54** 4728–4734